JET-R(95)08

Comparison between JET Profile Data and the Predictions of a Transport Model based on ITG and Trapped Electron Modes

M Fröjdh[1], J Christiansen, P Strand[1], J Weiland[1].

JET Joint Undertaking, Abingdon, Oxfordshire, OX14 3EA, UK.
[1] Institute for Electromagnetic Field Theory and Plasma Physics (Euraton–NFR Association),
Chalmers University of Technology, Göteborg, Sweden.

November 1995

Abstract

The predictions of a reactive drift wave model for anomalous transport in tokamaks, [Nucl. Fusion **30**, 983, 1990], is compared with JET profile data, using two different approaches. An interpretative approach is used to compare the radial heat fluxes under approximate steady-state conditions. For the considered steady states, taken from seven auxiliary heated JET discharges in various regimes, the predicted total heat flux tends to be over-estimated in the inner parts or under-estimated in the outer parts of the good confinement region (approximately between $q=1$ and $q=2$). A predictive approach is used to compare the density and temperature profiles of five L-mode discharges. These results are in good agreement with experiments (in the good confinement region the relative errors in the temperature profiles are $\leq 20\%$ and in the density profile approximately $\leq 25\%$). The interpretative code TRANSP is used to obtain the experimental profile data.

I. INTRODUCTION

No theory-based description for energy and particle transport in tokamak plasmas can today reproduce the whole range of experimental results. Many theories about the observed so-called anomalous transport are based on the assumption that small-scale instabilities generate turbulence which leads to transport. Often in these theories, a selection of what is thought to be the most relevant instabilities has been made. Recently, data from several JET experiments in different regimes were used to assess some of the theory-based transport models [1,2]. In the present paper, a reactive drift wave model for tokamak transport [3] is compared with experimental results from JET. Different versions of this model have been reported in the past [3-7]. In the present comparison we use a version where the transport is driven by the toroidal ion temperature gradient (ITG) mode and the collisionless trapped electron (CTE) mode. This model has previously been used to study linear stability and radial transport profiles [3,8], marginal stability [9], enhanced confinement regimes [10], transport for flat density profiles [11] and transport pinch effects [12] (corresponding to non-diagonal terms in a diffusion matrix). In the present study, we first focus on the perpendicular heat fluxes, comparing these with experimental results from discharges in various regimes. Analysed JET-data, as given from the interpretative code TRANSP, are used to obtain the experimental heat fluxes. We then use a transport simulation code to predict the density and temperature profiles for a series of L-mode discharges. These profiles are compared with the corresponding experimental profiles from TRANSP.

One way of assessing a transport model is to compare its predicted radial transport profiles with the corresponding experimental profiles [1,2]. The experimental profiles are then inferred from diagnostic data, local conservation laws and physics modelling of sources and losses. Many theories have proved incapable of reproducing the right trend of the experimental profiles, even though they may agree with the experiments in other respects.

One advantage of such an interpretative comparison is that it involves predicted physical quantities on a relatively low level in the transport model. One disadvantage is, however, that the compared transport may be sensitive to uncertainties in the experimental data. Another usual comparison method is to carry out transport code simulations [12-14]. This allows for a more consistent investigation of a transport model. However, the compared quantities (e.g. the density and temperature profiles) may then be rather insensitive to the details of the considered model. As a consequence, several models with different physics descriptions may lead to similar predictive results [15].

In the present report, we use an interpretative comparison method for a selection of JET discharges in various regimes. We then use a predictive or simulative comparison method for a series of L-mode JET discharges. The transport model investigated is a higher moment fluid model in which a combination of the toroidal branch of the ITG mode and the CTE mode drives the transport [3]. A modified mixing length estimate plays a central role in this model whereas the parallel ion dynamics are neglected. More details are presented in Section II. The interpretative part of the comparison is described in Sections III and IV. In Section III the diagnostic techniques and the processing of the measured JET data into "experimental" heat fluxes are briefly described. In Section IV the differences between the theoretical and the experimental profiles of the total heat flux, the ion heat flux and the electron heat flux are presented and discussed. The saturation level estimate of the model and the reliability of the obtained results are also discussed in this section. The predictive part of the comparison is then described in the following two sections. The transport modelling is described in Section V together with some numerical considerations. In Section VI the results of the predictive comparison are presented. Finally, the conclusions regarding both the interpretative and the predictive comparisons are summarized in Section VII.

II. A REACTIVE DRIFT WAVE MODEL FOR TOKAMAK TRANSPORT

In this model [3], the transport is driven by turbulence which is generated by small-scale instabilities, described as a combination of the toroidal ITG-mode (also called the toroidal η_i mode) and the CTE-mode. The linear fluctuations (in density, temperature and electrostatic potential) are governed by fluid equations and the quasi-neutrality condition (see appendix). All unstable fluctuations lead to transport and their contributions are superposed. The net transport across the magnetic field lines is obtained by using quasi-linear theory and a saturation level estimate.

The quasi-linear perpendicular heat flux (or energy flux) may be defined as

$$\vec{q}_j = \frac{3}{2}\sum_k \delta p_{j,k}(\delta \vec{v}_{j,k})^* + \text{c.c.} \qquad (1)$$

where the perturbative drift is taken as the perpendicular $\vec{E}\times\vec{B}$ drift and the sum over wave numbers is replaced by a normalization constant, assuming an average wave number k. This average wave number represents the inverse correlation length. The wave number subscript, k, is in the following suppressed whereas the subscript j denotes particle species (electrons or ions). The flux may be divided as

$$\vec{q}_j = \frac{3}{2}C\,\mathrm{Re}(\delta p_j\,\delta \vec{v}_E^{\,*}) = \frac{3}{2}Cn_j\,\mathrm{Re}(\delta T_j\,\delta \vec{v}_E^{\,*}) + \frac{3}{2}CT_j\,\mathrm{Re}(\delta n_j\,\delta \vec{v}_E^{\,*}) \qquad (2)$$

corresponding to a conductive and a convective flux. In terms of diffusivities, we may write this as

$$\vec{q}_j = -\chi_j n_j \nabla T_j - \frac{3}{2} D_j T_j \nabla n_j \qquad (3)$$

where

$$\chi_j = \frac{\frac{3}{2}C\ \mathrm{Re}(\delta T_j \delta v_E^*)}{-|\nabla T_j|} \tag{4}$$

$$D_j = \frac{C\ \mathrm{Re}(\delta n_j \delta v_E^*)}{-|\nabla n_j|} \tag{5}$$

In this report, however, neither the conductive nor the convective part of the heat flux is compared separately with the corresponding experimental heat flux. Note that the normalization constant (C) has been included in χ_j and D_j in (3). This constant was found to be close to one, for modes with $k^2\rho_s^2 = 0.1$ (corresponding to the most unstable ITG modes), in a comparative study of quasi-linear and non-linear transport, based on an ideal toroidal ITG-mode model [6]. In the rest of this report, C=1 is therefore assumed (as well as $k^2\rho_s^2 = 0.1$). In the quasi-linear heat flux $\vec{q}_j$ above, all fluctuating quantities except one can be eliminated by using the fluid equations and the quasi-neutrality condition. The saturation amplitude of the remaining fluctuating quantity can then be obtained by assuming that the convective $\vec{E}\times\vec{B}$ non-linearity in the energy equation is balanced by the linear growth

$$\gamma\, \delta T_j \sim \delta\vec{v}_E \cdot \nabla\, \delta T_j \tag{6}$$

and that ∇ in this relation can be replaced by an average k, representing the inverse correlation length. Non-linear isotropization ($k_x = k_y = k$) is also usually assumed. A saturation level estimate for the electrostatic potential is then obtained as

$$\delta\phi \sim \frac{B_0}{ck^2}\gamma \qquad \text{or} \qquad \frac{e\delta\phi}{T_e} = \frac{\gamma}{\omega_{*e}} \frac{1}{kL_{ne}} \tag{7}$$

which can also be regarded as a modified mixing length estimate. The modification is proportional to the growth rate. This means, however, that the fluctuation level may be under-estimated when the dominating mode is close to marginal stability. Otherwise, this estimate has been found to correlate reasonably well with the corresponding simulated non-linear fluctuation amplitude in toroidal ITG-mode models [6,7]. If the described saturation level estimate is used in the quasi-linear heat flux above, one may rewrite the latter as (with C=1 assuming $k^2\rho_s^2 = 0.1$)

$$\vec{q}_j = -\chi_j n_j \nabla T_j - \frac{3}{2} D T_j \nabla n_j \tag{8}$$

where

$$\chi_i = \frac{3}{2}\frac{1}{\eta_i}\left[\eta_i - \frac{2}{3} - (1-f_t)\frac{10}{9\tau}\varepsilon_n - \frac{2}{3}f_t\Delta_i\right]\frac{\gamma^3/k_x^2}{\left(\omega_r - \frac{5}{3}\omega_{Di}\right)^2 + \gamma^2} \tag{9}$$

$$D = f_t\Delta_n\frac{\gamma^3/k_x^2}{\omega_{*e}^2} \tag{10}$$

$$\chi_e = \frac{3}{2}f_t\frac{1}{\eta_e}\left[\eta_e - \frac{2}{3} - \frac{2}{3}\Delta_e\right]\frac{\gamma^3/k_x^2}{\left(\omega_r - \frac{5}{3}\omega_{De}\right)^2 + \gamma^2} \tag{11}$$

where

$$\begin{aligned}\Delta_i = \frac{1}{N}\{ |\hat{\omega}|^2\Big[|\hat{\omega}|^2(\varepsilon_n - 1) + \hat{\omega}_r\varepsilon_n\left(\frac{14}{3} - 2\eta_e - \frac{10}{3}\varepsilon_n\right) \\ + \frac{5}{3}\varepsilon_n^2\left(-\frac{11}{3} + 2\eta_e + \frac{7}{3}\varepsilon_n\right) - \frac{5}{3\tau}\varepsilon_n^2\left(1 + \eta_e - \frac{5}{3}\varepsilon_n\right)\Big] \\ + \frac{50}{9\tau}\hat{\omega}_r\varepsilon_n^3(1-\varepsilon_n) - \frac{25}{9\tau}\varepsilon_n^4\left(\frac{7}{3} - \eta_e - \frac{5}{3}\varepsilon_n\right)\}\end{aligned} \tag{12}$$

$$\Delta_e = \frac{1}{N}\{ |\hat{\omega}|^2\Big[|\hat{\omega}|^2(\varepsilon_n - 1) + \hat{\omega}_r\varepsilon_n\Big(\frac{14}{3} - 2\eta_e - \frac{10}{3}\varepsilon_n\Big)$$
$$+ \frac{5}{3}\varepsilon_n^2\Big(-\frac{8}{3} + 3\eta_e + \frac{2}{3}\varepsilon_n\Big)] + \frac{50}{9}\hat{\omega}_r\varepsilon_n^3(\varepsilon_n - 1)$$
$$+ \frac{25}{9}\varepsilon_n^4\Big(\frac{7}{3} - \eta_e - \frac{5}{3}\varepsilon_n\Big)\} \tag{13}$$

$$\Delta_n = \frac{1}{N}\Big\{ |\hat{\omega}|^2 (1 - \varepsilon_n) - \hat{\omega}_r\varepsilon_n\Big(\frac{14}{3} - 2\eta_e - \frac{10}{3}\varepsilon_n\Big)$$
$$- \frac{5}{3}\varepsilon_n^2\Big(-\frac{11}{3} + 2\eta_e + \frac{7}{3}\varepsilon_n\Big)\} \tag{14}$$

$$N = \Big(\hat{\omega}_r^{\,2} - \hat{\gamma}^{\,2} - \frac{10}{3}\hat{\omega}_r\varepsilon_n + \frac{5}{3}\varepsilon_n^2\Big)^2 + 4\,\hat{\gamma}^{\,2}\Big(\hat{\omega}_r - \frac{5}{3}\varepsilon_n\Big)^2 \tag{15}$$

The eigenvalues, $\omega = \omega_r + i\,\gamma$, can be determined from a dispersion relation:

$$\frac{\omega_{*e}}{N_i}\Big[\omega(1 - \varepsilon_n) - \Big(\frac{7}{3} - \eta_i - \frac{5}{3}\varepsilon_n\Big)\omega_{Di}$$
$$-k^2\rho_s^2(\omega - \omega_{*i}(1 + \eta_i))\Big(\frac{\omega}{\omega_{*e}} + \frac{5}{3\tau}\varepsilon_n\Big)] =$$
$$f_t\frac{\omega_{*e}}{N_e}\Big[\omega(1 - \varepsilon_n) - \Big(\frac{7}{3} - \eta_e - \frac{5}{3}\varepsilon_n\Big)\omega_{De}\Big] + 1 - f_t \tag{16}$$

where

$$N_j = \omega^2 - \frac{10}{3}\omega\omega_{Dj} + \frac{5}{3}\omega_{Dj}^2 \tag{17}$$

The diffusivities above were derived in [3] and [8], except for the factor 3/2 which we in this report have chosen to include in the thermal diffusivities χ_j. All unstable eigenvalues should be taken into account in the diffusivities above, even though this is not shown explicitly (their contributions to the transport should be superposed). The notation used in the transport coefficients above is explained in greater detail in the appendix where also the governing fluid equations are given.

III. EXPERIMENTAL HEAT FLUXES

To be able to compare the predicted heat flux, as given from the reactive drift wave model, with the experimental heat flux, a certain degree of physics modelling is necessary. TRANSP, a transport analysis code [16], can provide the necessary transformation of the measured quantities into comparable transport related quantities. This section describes the derivation of experimental steady-state heat fluxes and discusses some of the limitations of the comparison and the selection of discharges.

In TRANSP, experimental data are used whenever possible to define plasma parameters. In the present (interpretative) comparison, we require that charge exchange recombination spectroscopy data are available so that e.g. the ion temperature profile can be determined. The electron temperature profile is obtained from electron cyclotron emission spectra, the electron density profile from microwave interferometry and the radiated power density profile from bolometry. Measurements of the plasma boundary and shape are in TRANSP used by an MHD equilibrium solver to determine the magnetic flux surface geometry. Physics modelling codes, based on Monte Carlo techniques, are used to calculate the auxiliary power (ICRH and/or NBI) and the particle deposition profiles. The conservation laws for energy and particles are then used to determine the local transport quantities. We will in this part of the report concentrate mainly on the heat flux (or energy flux), q_j, which fulfils the equation

$$\frac{\partial W_j}{\partial t} + \int \vec{q_j} \cdot d\vec{S} = P_j \qquad (18)$$

where P_j is the total heating rate inside a magnetic flux surface, including all sources/sinks and the collisional equipartion. For steady-state conditions, the flux surface averaged perpendicular heat flux is then obtained as

$$< q_j(\rho) > = \frac{P_j(\rho)}{S(\rho)} \tag{19}$$

where $S(\rho)$ is the magnetic flux surface at position ρ. The positional coordinate ρ is defined as the square root of the normalized poloidal magnetic flux. The derived heat flux consists of both conductive and convective contributions and can also be written as

$$< \vec{q_j} > = < -\chi_j n_j \nabla T_j - \frac{3}{2} D_j T_j \nabla n_j > \tag{20}$$

where χ_j and D_j are the thermal and particle diffusivities. All non-diffusive contributions to the heat flux are assumed to be negligible. The experimental heat flux (20) is similar to the theoretical heat flux (8) except that the latter is not flux surface averaged. This difference is due to taking the strongly ballooning limit in the reactive drift wave model. The tranport is then evaluated at a point on the flux surface where the poloidal angle is zero. This approximation is not expected to affect the scaling properties of the predicted transport in a determining way. However, the magnitude is affected. The total heat flux, which is the superposition of the ion and electron heat fluxes,

$$< q_{tot} > = < q_i > + < q_e > \tag{21}$$

will also be considered in our comparison. It is the relevant quantity to study whenever the ion and electron channels cannot be separated with sufficient accuracy. This may happen whenever the energy exchange rate between electrons and ions is uncertain (e.g. if the ion and electron temperatures are very close). Other limitations in our study are imposed by the lack of diagnostic information from the edge region or by the existence of MHD related activities in the inner region of the discharge. For most discharges the comparison is therefore restricted to the intermediate region of the plasma, approximately between ρ=0.4 and ρ=0.8, corresponding to $q \approx 1$ and $q \approx 2$. We will refer to this region as "the good confinement region". Constraints are also imposed by the restricted validity of the considered transport model, the reactive drift wave model. A low beta value and a low collisionality are required. However, these conditions are usually easily fulfilled in the JET discharges considered in this report.

The following selection of TRANSP processed JET pulses was made for the comparison of heat fluxes: #17749 (pellet fuelled ICRH discharge), #19691 (L-mode discharge), #19739 (monster sawtooth discharge), #20981 (hot ion discharge), #25432, #26095 and #26705. In order to minimize the influence of random errors, several steady-state events were selected from every discharge. Various types of confinement regimes, in both the L and H-mode, can be found in these discharges. Some of the main characteristics are shown in Table I.

IV. INTERPRETATIVE RESULTS AND DISCUSSION

In this section the heat flux profiles of the reactive drift wave model and of the experiments are compared. The results have been mapped against a magnetic flux surface coordinate, defined as the square root of the normalized poloidal magnetic flux. For most JET discharges, this is approximately equivalent to a mapping against the normalized minor radius. In all figures, we concentrate on the shape (or trend) of the majority of the profiles when discussing the correlation between theory and experiment. The magnitude of the heat fluxes should not be compared since the reactive drift wave model does not predict flux surface averaged quantities (the predicted transport level is therefore uncertain).

A. Total heat flux

For all considered steady-state time events, the ratio of the theoretical and experimental total heat fluxes is shown in Fig. 1. For agreement, a constant ratio at some level is required. For the majority of profiles, this is approximately true for a limited interval of the magnetic flux surface coordinate. The trend for the whole of the region where our comparison is expected to hold (approximately between $\rho=0.4$ and $\rho=0.8$) indicates, however, disagreement. The reason for this disagreement is difficult to determine since the profiles can be very different. However, for many steady states the ratios are larger in the inner parts of the good confinement region than in the intermediate or outer parts. This result is similar to previous assessments of transport models where the toroidal ITG-mode is a main ingredient. We may interpret this lack of radial correlation as if there is too little predicted heat flux in the outer parts or too much predicted heat flux in the inner parts of the good confinement region. The toroidal ITG-mode can be responsible for much of this radial decorrelation since it leads to a large heat flux in the inner good confinement region where the temperature gradient tends to be large in the, predominantly, high-performance discharges considered in this comparison. To improve the obtained result, other effects which influence the ITG-mode stability or which give rise to other instabilities which dominate more towards the edge could be introduced into the model. For instance, impurity ions may have a stabilizing influence on the ITG-mode, especially in regions where η_i and ε_n are large (often fulfilled in the inner good confinement region). Another improvement could be to develop the saturation level estimate further, by for instance using different estimates in different regimes. In the interval $\rho=0.6$ to $\rho=0.8$ the correlation between experiment and theory improves. In this region, modes in the electron drift direction are likely to be excited. Below, we separate the total heat flux into an ion and an electron component.

B. Ion heat flux

Fig. 2 shows ratios of theoretical and experimental ion heat fluxes for all the considered steady-state time events. For many of the profiles (but not for all), the theoretical ion heat flux is over-represented in the bulk plasma (where the ITG-mode is usually unstable) or under-represented in the edge plasma. The radial dependence of the ion energy transport was found to be very sensitive to where the unstable modes are most strongly excited. This strong dependence on the growth rate, or more precisely on the last factor in the expression for the thermal conductivity (9), is illustrated in Figs 3-4 for one discharge. Often, the $T^{3/2}$ dependence of χ in drift wave models is thought to be responsible for the decreasing trend with respect to radius. However, in the reactive drift wave model, the radial dependences of the linear growth rates determine much of the radial trend of the transport coefficients. Most of this dependence originates from the used saturation level estimate. As a consequence, when an instability is dominated by the ITG-mode, the ion temperature gradient, in particular, determines the radial trend of the heat flux profile. The peak of the heat flux profile in the bulk plasma is then usually a consequence of the often bell-shaped ion temperature profile, typical of auxiliary heated discharges. However, for broader temperature profiles these peaks tend to disappear and the agreement improves. When an instability is dominated by the CTE-mode, on the other hand, both the electron temperature gradient and the density gradient as well as the fraction of trapped electrons drive the instability. In most cases, this instability is then excited for larger radial values where the transport accordingly increases. Another effect which can influence the radial dependence of the predicted transport is the explicit occurrence of non-diagonal terms in the expression for the thermal diffusivity, χ. For the considered discharges, we found, however, that these were usually of minor importance in the good confinement region. It should also be pointed out that impurity ions (not included in the considered transport model) with a broader density profile than the main ions could lead to an increased η_i, and accordingly an increased χ_i , towards the edge.

C. Electron heat flux

The profiles of the ratio of the predicted and experimental electron heat fluxes are shown Fig. 5. For most of the considered steady states, the predicted electron heat flux is too large in the outer part of the good confinement region. However, some profiles show a fairly good agreement between theory and experiment. These results correspond to smooth temperature profiles and moderate auxiliary heating. However, for other situations with steeper temperature profiles, the predicted heat flux tends to be too large towards the edge and may frequently be directed inwards in the bulk plasma (as opposed to the experimental flux). This predicted energy pinch (inward transport) is of a convective nature and associated with a negative particle diffusion coefficient. Also the convective part of the ion heat flux is then inwardly directed due to particle ambipolarity (however, the ion heat flux in this region is dominated by the large outwardly directed conductive transport). The predicted energy pinch requires a rather flat density profile and is emphasized by a steep temperature profile. This is often fulfilled in the bulk region where the ITG-mode dominates. The predicted pinch is therefore primarily driven by the ITG-mode. As for the ion transport, the trend of the electron transport radial profile is sensitive to the linear growth rates. It is worth noticing that the predicted electron transport, when dominated by an electron mode, usually has its maximum near the edge rather than in the bulk plasma. This leads to a radially increasing trend of the electron transport. The result depends on the fact that only the trapped part of the electrons drives the mode (it introduces a factor $f_t/(1-f_t)$ in the driving term for an instability, f_t being the fraction of trapped electrons). It can then be shown that, unless the density profile has strong gradients, the mode excitation is pushed more towards the edge region. If the ions were described similarly, introducing a fraction of trapped ions into the model and assuming that the passing ions contribute less to the transport, this would lead to a radially increasing ion heat flux profile.

D. Estimate of the saturation amplitude

As mentioned earlier, the predicted quasi-linear heat flux is highly dependent upon the used saturation amplitude estimate. The heat flux is proportional to the square of the saturation amplitude. When this amplitude is estimated it becomes proportional to the growth rate which therefore makes the transport sensitive to, for example, the details of the ion temperature gradient. In Fig. 6, the saturation estimate of $|\delta T_i / T_i|$ for shot #17749 is shown (this estimate follows from (7) and the linear relation between the potential and temperature perturbations in the fluid equations). This figure is an example showing that this estimate often leads to a turbulence level with a maximum in those parts of the good confinement region where the instabilities are most strongly excited, typically where the ion temperature gradient is largest. However, sometimes a smoother profile would be desirable in order to correlate with experimental observations.

E. Reliability of the obtained results

The result that the predicted heat fluxes are sensitive to the growth rates means that some of the details (the scale lengths) of the experimental profiles are relatively important for the outcome of the present comparison. This is one of the main arguments against using an interpretative comparison technique. In our case, the errors due to any uncertainties in the experimental profiles were minimized by restricting the comparison to include only the most well diagnosed discharges. For these discharges, a large number of steady-state events were studied and only the trend for the majority of the compared heat flux profiles was considered. Any random errors due to experimental uncertainties should therefore have been averaged out whereas systematic errors could still affect the result. Due to taking the strongly ballooning limit in the considered reactive drift wave model, the predicted transport could not be flux surface averaged. The magnitudes of the predicted heat fluxes were therefore uncertain which made a reliable systematic sensitivity analysis difficult to perform. However, an initial sensitivity analysis was carried out which indicated that it would be unlikely to obtain agreement by changing the experimental temperature and density profiles within the estimated experimental error bars. All other errors were then neglected. On the other hand, we note that a radially increasing χ_i was previously predicted for the JET shots #16063 and #17259 (see [3]) and for the L mode shot in [1] (see [17]), when averaged temperature and density profiles were used as input. We would also like to underline the fact that our results are based on a selection of steady states where a variety of confinement regimes are represented. Finally, we should mention that there are a number of effects which are not included in the considered transport model which could lead to different predictions. We have already mentioned impurity ions and trapped ions. Other effects may be due to beam ions, parallel ion dynamics, transit and drift resonances, electromagnetic effects, plasma rotation etc. The radial variation of the predicted transport could also be affected by toroidal couplings of the ion temperature gradient driven mode, leading to a correlation length that depends on radius [18].

V. PREDICTIVE TRANSPORT SIMULATIONS

In the previous part of the report, an interpretative comparison technique was adopted. Another way of evaluating the relevance of a transport model is to use it in a predictive transport code. The transport equations are then solved self-consistently, with particle and energy sources given by the experimental deposition profiles. The drift wave model described in Section II has been implemented in a transport code, see [10]. A modified version of this code, extended to include geometrical equilibrium properties relevant for JET discharges and using a different formulation of the transport equations, is used in the following to analyse a set of L-mode discharges.

A. Transport Equations

We solve for three channels of transport, P_i, P_e and n, where $n = n_i = n_e$ and the pressure terms are defined as $P_j = nT_j$. The temporal evolution of these profiles are modelled by the following set of equations [19,20] :

$$\frac{3}{2}\frac{1}{V'^{5/3}}\frac{\partial}{\partial t}\left(V'^{5/3}p_i\right)+\frac{1}{V'}\frac{\partial}{\partial \rho}\left\{V'\left(\langle \vec{q}_i \cdot \nabla\rho\rangle+\frac{3}{2}T_i\Gamma_n\right)\right\}=\langle S_i\rangle \qquad (22)$$

$$\frac{3}{2}\frac{1}{V'^{5/3}}\frac{\partial}{\partial t}\left(V'^{5/3}p_e\right)+\frac{1}{V'}\frac{\partial}{\partial \rho}\left\{V'\left(\langle \vec{q}_e \cdot \nabla\rho\rangle+\frac{3}{2}T_e\Gamma_n\right)\right\}=\langle S_e\rangle \qquad (23)$$

$$\frac{1}{V'}\frac{\partial}{\partial t}(V'n)+\frac{1}{V'}\frac{\partial}{\partial \rho}\{V'\Gamma_n\}=\langle S_n\rangle \qquad (24)$$

The notation for the geometrical quantities is conventional [21] with ρ as the toroidal flux surface label and where $V(\rho)$ is the volume inside a flux surface defined by ρ and $V'=\partial V/\partial\rho$. The source terms, $<S_i>$, $<S_e>$ and $<S_n>$, include both auxiliary heating and internally calculated contributions, such as resistive equilibration terms. The flux surface averaging operator is defined as

$$\langle ... \rangle=\frac{2\pi}{V'}\int_o^{2\pi}\sqrt{g}\,d\theta(...) \qquad (25)$$

where $\sqrt{g}$ is the Jacobian of the magnetic coordinate system used. The averaged radial fluxes are assumed to be in the following form (we now use a different definition of q_j than in the previous sections)

$$< \vec{q}_j \cdot \nabla\rho > = -\chi_j^{eff} n \frac{\partial T_j}{\partial \rho} < |\nabla\rho|^2 > \qquad (26)$$

$$\Gamma_n=-D^{eff}\frac{\partial n}{\partial \rho}\left\langle|\nabla\rho|^2\right\rangle \qquad (27)$$

The governing equations, (22-24), can be written in a compact matrix form. With $\vec{u}=(P_i,P_e,n)$, $\vec{S}=\left(\frac{2}{3}S_i,\frac{2}{3}S_e,S_n\right)$, together with a flux surface averaged transport matrix $<\chi_{ij}>$, and assuming $\partial V'/\partial t=0$ we have

$$\frac{\partial u_i}{\partial t} = \frac{1}{V'}\frac{\partial}{\partial \rho}\left\{ V' < |\nabla \rho|^2 > \left(\sum_{j=1}^{3} \langle \chi_{ij} \rangle \frac{\partial u_i}{\partial \rho} + \langle \Lambda_i \rangle u_i \right) \right\} + \langle S_i \rangle, i = 1,\ 2,\ 3 \qquad (28)$$

In this equation, the fluxes are divided into diffusive and convective contributions, as described in the following subsection. The following boundary conditions and initial values were used

$$\begin{cases} \left.\frac{\partial u_i}{\partial \rho}\right|_{\rho=o} = 0 \\ & i = 1,\ 2,\ 3 \\ \left.u_i\right|_{\rho=a} = g_i(t) \end{cases} \qquad (29)$$

$$u_i(\rho, 0) = f_i(\rho) \quad i = 1,\ 2,\ 3. \qquad (30)$$

Each transport calculation then consists of solving (28), using the boundary conditions and the initial values. It should be noted that this is done under the assumption of a constant geometry. One way of including the effects of a changing equilibrium configuration is to update the geometrical quantities $\left(V', < |\nabla \rho|^2 >\right)$ at every time step. In order to keep the conservative properties of (28) we then need to update the profiles consistently with the changing geometry. This is done by using adiabatic constraints [19] :

$$\begin{aligned} P_i^{new}(V')^{new5/3} &= P_i^{old}\left(V'^{old}\right)^{5/3} \\ P_e^{new}(V')^{new5/3} &= P_e^{old}\left(V'^{old}\right)^{5/3} \qquad (31) \\ n^{new}(V')^{new} &= n^{old}V'^{old} \end{aligned}$$

Both the geometry and the profiles are updated at every time step. Since the simulation code does not include an MHD equilibrium solver of its own, equilibrium quantities need to be accessed through interfacing external packages. In the present version of the code, IDENTC [22] equilibrium data are accessed through FLUSH [23] library routines. Source terms, boundary values and other quantities, not calculated internally by the simulation code, are taken from TRANSP [16].

B. Transport Coefficients

The transport coefficients defined in Section II are effective quantities, derived from quasi-linear fluxes. Since they are defined in this way, they will consist of parts which are not strictly diffusive or conductive in character. These parts can give negative transport coefficients, corresponding to pinches.

It may be convenient to express the fluxes in terms of a transport matrix [10]. The pinch effects will then appear as off-diagonal terms in the matrix. In this report, a slightly different approach is used, expressing the fluxes first as a sum of diffusive and convective terms:

$$n\chi_j^{eff}\frac{\partial Tj}{\partial\rho} = n\chi_j^{D}\frac{\partial T_j}{\partial\rho} + v_j^D n T_j,\ j = i,\ e \qquad (32)$$

$$D^{eff}\frac{\partial n}{\partial\rho} = D^{D}\frac{\partial n}{\partial\rho} + v_n^D n \qquad (33)$$

This formulation seems to be numerically more stable for flat and hollow profiles. Both formulations can be obtained from the effective diffusivities, expanding the scale length dependence in different ways.

It should also be noted that the transport coefficients of the reactive drift wave model are defined in the strongly ballooning limit. This prevents us from calculating proper flux surface averaged transport coefficients, see (25). Instead, a multiplying factor f_B is used,

$$\langle ... \rangle = f_B(...) \qquad (34)$$

This factor is given as input to the program and then held constant throughout the calculations.

In order to run the simulation code, a transport model which is valid over the whole plasma radius is required. Since the drift-wave transport coefficients tend to zero towards the axis, additional transport must be supplied in this region. This is done by using constant artificial transport coefficients out to a given radius. With

$$\begin{cases} \chi_i = \chi_i^{art} + f_B \ \chi_i^D \\ \chi_e = \chi_e^{art} + f_B \ \chi_e^D \\ D = D^{art} + f_B \ D^D \end{cases} \tag{35}$$

the transport matrix of (28) can be written as

$$(\chi_{ij}) = \begin{pmatrix} \chi_i & o & T_i(D-\chi_i) \\ o & \chi_e & T_e(D-\chi_e) \\ o & o & D \end{pmatrix} \tag{36}$$

and the convectice term in this equation can be written as

$$(\Lambda_i) = f_B \begin{pmatrix} V_i + V_n \\ V_e + V_n \\ V_n \end{pmatrix} \tag{37}$$

The artificial transport coefficients are held at constant values out to a given radius throughout the simulations. Their values are thus not changed between the different shots, once a set of values has been decided upon. The following values were used in our simulations

$$\chi_i^{art} = 2\,\chi_e^{art} = 4D^{art} = 0.5\,, \quad r/a \le 0.3 \tag{38}$$

However, the step transition to zero at r/a = 0.3 was softened slightly to avoid step discontinuities.

C. Numerical Implementation

The conservative properties of (28) must remain also in the numerical treatment. This can be achieved by a proper centring of the finite differences used for the space derivatives. Using a fully implicit approach and defining half-mesh values as $f_{\rho+1/2} = \frac{1}{2}\left(f_{\rho+1} + f_\rho\right)$ we have

$$u_{i,\rho}^{t+1} - u_{i,\rho}^{t} = \frac{\Delta t}{V'_\rho(\Delta\rho)^2}\times$$

$$\left\{ V'_{\rho+1/2}\langle|\nabla\rho|^2\rangle_{\rho+1/2}\left[\sum_{j=1}^{3}\chi_{ij,\rho+1/2}^{t+1}\left(u_{j,\rho+1}^{t+1}-u_{j,\rho}^{t+1}\right) + \Delta\rho\,\Lambda_{i,\rho+1/2}^{t+1}\,u_{i,\rho+1/2}^{t+1}\right] - \right. \qquad (39)$$

$$\left. -V'_{\rho-1/2}\langle|\nabla\rho|^2\rangle_{\rho-1/2}\left[\sum_{j=1}^{3}\chi_{ij,\rho-1/2}^{t+1}\left(u_{j,\rho}^{t+1}-u_{j,\rho-1}^{t+1}\right) + \Delta\rho\,\Lambda_{i,\rho-1/2}^{t+1}\,u_{i,\rho-1/2}^{t+1}\right]\right\} + S_{i,\rho}^{t}$$

Here, Δt and $\Delta\rho$ are the step lengths in time and space, respectively. Equation (39) can also be written as the tri-diagonal system

$$\alpha^{t+1}\,\bar{u}_{\rho+1}^{t+1} + \beta^{t+1}\bar{u}_{\rho}^{t+1} + \gamma^{t+1}\bar{u}_{\rho-1}^{t+1} = \bar{\delta}_{\rho}^{t} \qquad (40)$$

where the matrices α^{t+1}, β^{t+1} and γ^{t+1} are functions of the temperature and density profiles, as well as their scale lengths, at the implicit time t+1. There are several ways of dealing with the non-linear dependence in α, β and γ. We have employed a predictor-corrector approach:

$$\alpha^{t}\,\vec{u}_{\rho+1}^{\,t*} + \beta^{t}\,\vec{u}_{\rho}^{\,t*} + \gamma^{t}\,\vec{u}_{\rho-1}^{\,t*} = \vec{\delta}_{\rho}^{\,t} \qquad \text{(predictor)} \qquad (41)$$

$$\alpha^{t*}\,\vec{u}_{\rho+1}^{\,t+1} + \beta^{t*}\,\vec{u}_{\rho}^{\,t+1} + \gamma^{t*}\,\vec{u}_{\rho-1}^{\,t+1} = \vec{\delta}_{\rho}^{\,t} \qquad \text{(corrector)} \qquad (42)$$

Both the predictor and corrector steps are tri-diagonal equations which can be solved using standard techniques. The method used in our simulation code is known as the 'double-sweep' [20] method, or Tomas algorithm [24]. Essentially, it consists of a Gaussian elimination, incorporating the boundary conditions.

Inserting the ansatz

$$\vec{u}_{\rho}^{\,t+1} = \varepsilon_{\rho}\, \vec{u}_{\rho+1}^{\,t+1} + \vec{F}_{\rho} \tag{43}$$

or its inverse

$$\vec{u}_{\rho+1}^{\,t+1} = \varepsilon_{\rho}\, \vec{u}_{\rho}^{\,t+1} + \vec{F}_{\rho} \tag{44}$$

into the tri-diagonal system above will give us recurrence relations for ε and $\vec{F}$ in terms of α, β, γ, δ. Using the boundary values, see (29), we can then solve for $\{\bar{u}\}^{t+1}$.

The ITG-modes, as described by the reactive drift wave model, are often close to marginal stability in the inner half of the plasma. This can lead to numerical instabilities [13]. Small changes in the gradients can then lead to large changes in the fluxes and, in turn, enhance the changes in the gradients. In order to avoid this behaviour, a smoothing of the inverse scale lengths has been introduced before the calculations of the transport coefficients. This smoothing is performed by a running-average method, applied twice to the relevant inverse scale length according to the formula

$$f_{\rho} = (f_{\rho-1} + 2\, f_{\rho} + f_{\rho+1})/4 \tag{45}$$

This stabilises the numerical scheme, without significantly changing the results of the simulations.

V I PREDICTIVE RESULTS AND DISCUSSION

The described simulation code has been used to predict the temporal evolution of the density and temperature profiles. Initial values were obtained from TRANSP, as well as time dependent sources and boundary conditions. The code has so far been used mainly to simulate L-mode discharges, see Table II. In the illustrations (Figs 7-12) of this section, x stands for the normalized minor radius (x=r/a).

In order to evaluate the results of the simulations, the following quality measure [13] for the temperature profiles was introduced

$$\frac{\sigma_{Tj}}{T_j} = \frac{\sqrt{\sum_{l=1}^{N} (T_{l,j}^{\ pred} - T_{l,j}^{\ exp})^2 / N}}{T_j^{\ max}} \quad , \ j=i,e \qquad (46)$$

with a similar measure defined for the density profile. Here, T_j^{max} is the maximum temperature along the profile and the sum is over all spatial grid points along the minor radius.

In Table III, the time average of the quality measures σ_{Ti}/T_i , σ_{Te}/T_e and σ_n/n for all shots are presented, using different flux surface averaging factors, f_B. The time evolution of the the different quality measures for shot #19691 are presented in Fig. 7. This figure indicates that the flux surface averaging factor has a rather constant influence on the resulting profiles, except in the initial phase of the simulations.

Figs 8-10 show the relative errors in the ion and electron temperature profiles and in the density profile, for all of the considered L-mode discharges. The profiles shown are taken at the end of the simulation time interval for each shot (for more details, see table III and the figure captions). We note the good agreement in the good confinement region (≤20% relative errors in the two temperature profiles and approximately ≤25% in the density profile). All these results were obtained with the flux surface averaging factor, f_B , equal to unity (i.e. the transport coefficients were not flux surface averaged). The relatively large discrepancies closer to the axis (inside the q=1 surface) should not be regarded as a deficiency of the reactive drift wave model, but rather as an indication of the quality of the artificial diffusivities used. In the good confinement region, the predicted profiles are rather insensitive to the details of this modelling.

It should be stressed that no effects of impurities have been included in the present version of the code. Inclusion of impurities would provide a better description of the densities when the simple condition $n_i = n_e$ is relaxed. Without impurities the predicted density tends to an average value of the experimental electron and ion densities when it is free to evolve self-consistently. However, the boundary condition ($n= n_i = n_e$) will impede this tendency in the outer part of the plasma as well as affect the density scale length and hence the transport properities of that region.

In Fig. 11, the predicted profiles of shot #19691 at the experimental time 55.8s (corresponding to 2.8s in the simulation) are compared with a ±10% error estimate from the corresponding TRANSP data (shown as dotted lines). This figure suggests that, if the experimental temperature profiles are changed 10-20% and the experimental density profile is changed approximately 25%, the experimental fluxes can be reproduced by the transport simulation code. Results for the other L-mode shots are similar.

Finally, in Fig. 12 we show that the effective ion thermal diffusivity has a pronounced radial growth up to $r/a \approx 0.8$, for shot #19691 (t=55.8s). This tendency can be explained by the self-consistently calculated profiles being close marginal stability in the inner parts of the good confinement region.

VII. CONCLUSIONS

A reactive drift wave fluid model for tokamak transport [3] has been compared with profile data from JET. Both an interpretative and a predictive comparison technique have been employed.

The considered discharges in the interpretative comparison included time periods with high confinement properties, accompanied by large temperature gradients. For steady-state conditions, the predicted heat fluxes were compared with the corresponding experimental heat fluxes as given from TRANSP. For our selection of steady states, the predicted total heat flux tends to be too large in the bulk region compared to the edge region. This is caused by a large ion heat flux in the bulk plasma, in most cases driven by the toroidal ITG-mode. Alternatively, the result may be interpreted as a lack of transport (or instabilities that can match the ITG-mode) in the edge region. The comparison indicates that if trapped rather than free ions would have been used in the reactive drift wave model, to drive the ion transport, a better radial scaling of the ion heat flux would result. The ion heat flux profile would then become more similar to the electron heat flux profile. The latter is better correlated with experiments in the sense that it usually increases with radius. However, the electron heat flux seems to increase too much and is often inwardly directed in the bulk plasma in contrast to the experimental results (this pinch is usually driven by the ITG-mode). It was found that the trends of both the ion and electron heat flux profiles, predicted by reactive drift wave model, are to a large extent determined by the position along the radius where the modes are most strongly excited (where the growth rate is largest). Much of this dependence is a consequence of the used saturation level approximation which depends on the growth rate and therefore introduces a strong growth rate dependence in the transport coefficients. This sensitivity means that the predicted transport profiles are relatively dependent upon details of the experimental profiles, or on any effect which may change the linear stability properties. However, in this study, the influence from random uncertainties of the experimental profiles on the overall result should have been averaged out since only the trend for a large number of steady states was considered. The explicit dependence on non-diagonal terms in the diffusivities was, on the other hand, generally of less importance for the radial behaviour of the heat fluxes in the good confinement region.

The transport model has also been evaluated by means of predictive transport code simulations. These simulations were carried out for a series of L-mode discharges. Starting from initial values provided by the interpretative transport analysis code TRANSP, the temporal evolution of the ion temperature, electron temperature and density profiles were followed under the assumption of quasi-neutrality. Since the considered reactive drift wave model is formulated in the strongly ballooning limit a proper flux surface averaging of the transport coefficients could not be performed. In order to take the effects of a finite mode width into account a correction factor was introduced. In the region of the tokamak plasma for which the reactive drift wave model is intended (the good confinement region), encouraging results were obtained. The relative errors in the temperature profiles were ≤20% and in the density profile approximately ≤25%. A profile averaged error measure was introduced in the predictive comparison. This measure could increase in the beginning of the simulations but, as the profiles have had time to develop self-consistently, this error measure did usually not increase with time. This is encouraging because at the same time the profiles changed dynamically.

APPENDIX

Some of the notations used in the reactive drift wave model in Section II are explained below. The subscript j denotes particle species, j=i,e.

$$\eta_j = \frac{L_n}{L_{Tj}} \tag{A1}$$

$$f_t = \sqrt{\frac{2\varepsilon}{(1+\varepsilon)}} \quad \text{, fraction of trapped electrons} \tag{A2}$$

where

$$\varepsilon = \frac{r}{R} \tag{A3}$$

$$\omega_{Dj} = \vec{k} \cdot \vec{v}_{Dj} = k_y v_{Dj} \quad \text{, magnetic drift frequency} \tag{A4}$$

where

$$\vec{v}_{Dj} = \frac{T_j}{m_j \Omega_{cj}} \left(\frac{\vec{B}_0}{B_0} \times \frac{\nabla B_0}{B_0} + \frac{\vec{B}_0}{B_0} \times \left(\left(\frac{\vec{B}_0}{B_0} \cdot \nabla \right) \frac{\vec{B}_0}{B_0} \right) \right) \tag{A5}$$

$$\Omega_{c\,i,e} = \pm \frac{eB_0}{m_{i,e}c} \quad \text{, cyclotron frequency} \tag{A6}$$

$$\rho_s = \frac{\sqrt{T_e/m_i}}{\Omega_{ci}} \quad \text{, Larmor radius} \tag{A7}$$

$$\rho_j = \frac{v_{thj}}{\Omega_{cj}} \quad \text{, Larmor radius} \tag{A8}$$

$$v_{thj} = \sqrt{\frac{T_j}{m_j}} \quad \text{, thermal velocity} \tag{A9}$$

$$\omega_{*j} = \vec{k} \cdot \vec{v}_{*j0} = -\frac{k_y v_{thj}\rho_j}{L_n}\text{, diamagnetic drift frequency} \qquad (A10)$$

$$\varepsilon_n = \frac{\omega_{Dj}}{\omega_{*j}} = \frac{2L_n}{L_B} \qquad (A11)$$

$$\tau = \frac{T_e}{T_i} \qquad (A12)$$

$$\hat{\omega} = \frac{\omega}{\omega_{*e}} \qquad (A13)$$

The linearized fluid equations are given below. For ions, the linearized fluid velocities are

$$\delta\vec{v}_{i\perp} = \delta\vec{v}_E + \delta\vec{v}_{pi} + \delta\vec{v}_{*i} + \delta\vec{v}_{\pi i} \qquad (A14)$$

which inserted into the continuity and energy equations give

$$\omega\frac{\delta n_i}{n_i} = (\omega_{Di} - \omega_{*i})\frac{e\delta\phi}{T_i} + \omega_{Di}\frac{\delta p_i}{p_i} - k_\perp^2\rho_i^2(\omega - \omega_{*i}(1+\eta_i))\frac{e\delta\phi}{T_i} \qquad (A15)$$

$$\omega\frac{\delta p_i}{p_i} = -\omega_{*i}(1 + \eta_i)\frac{e\delta\phi}{T_i} + \frac{5}{3}\omega_{Di}\left(\frac{e\delta\phi}{T_i} + 2\frac{\delta p_i}{p_i} - \frac{\delta n_i}{n_i}\right) \qquad (A16)$$

Similarly, for the trapped electrons (no FLR-terms)

$$\delta\vec{v}_{\perp e} = \delta\vec{v}_E + \delta\vec{v}_{*e} \qquad (A17)$$

which give

$$\omega\frac{\delta n_e}{n_e} = -(\omega_{De} - \omega_{*e})\frac{e\delta\phi}{T_e} + \omega_{De}\frac{\delta p_e}{p_e} \qquad (A18)$$

$$\omega\frac{\delta p_e}{p_e} = \omega_{*e}(1 + \eta_e)\frac{e\delta\phi}{T_e} + \frac{5}{3}\omega_{De}\left(-\frac{e\delta\phi}{T_e} + 2\frac{\delta p_e}{p_e} - \frac{\delta n_e}{n_e}\right) \qquad (A19)$$

The quasi-neutrality condition reads

$$\frac{\delta n_i}{n_i} = (1-f_t)\frac{e\delta\phi}{T_e} + f_t\frac{\delta n_e}{n_e} \qquad \text{(A20)}$$

where f_t is the fraction of trapped electrons and $\delta n_e/n_e$ is the density response for trapped electrons only.

ACKNOWLEDGMENTS

This work was undertaken under Task Agreement No. 401 between the JET Joint Undertaking and the Swedish Natural Science Research Council (NFR).

M.F. and P.S. gratefully acknowledge the hospitality of the JET Data Analysis and Modelling Unit as well as the assistance and encouragement given by Dr D. Muir.

REFERENCES

[1] Connor J W, Maddison G P, Wilson H R, Corrigan G, Stringer T E and Tibone F 1993 *Plasma Phys. and Control. Fusion* **35** 319

[2] Tibone F, Connor J W, Stringer T E and Wilson H R 1994 *Plasma Phys. and Control. Fusion* **36** 473

[3] Nordman H, Weiland J and Jarmén A 1990 *Nucl. Fusion* **30** 983

[4] Andersson P and Weiland J 1988 *Phys. Fluids* **31** 359

[5] Jarmén A, Andersson P and Weiland J, *Nucl. Fusion* **27** 941

[6] Nordman H and Weiland J 1989 *Nucl. Fusion* **29** 251

[7] Jarmén A and Nordman H 1992 *Plasma Phys. and Control. Fusion* **34** 749

[8] Weiland J, Jarmén A and Nordman H 1989 *Nucl. Fusion* **29** 1810

[9] Nordman H and Weiland J 1992 *Nucl. Fusion* **32** 1653

[10] Weiland J and Nordman H 1991 *Nucl. Fusion* **31** 390

[11] Heikkilä A and Weiland J 1993 *Phys. Fluids* **B5** 2043

[12] Weiland J and Nordman H 1993 *Phys. Fluids* **B5** 1669

[13] Bateman G 1992 *Phys. Fluids* **B4** 634

[14] Kinsey J, Singer C, Cox D and Bateman G 1994 *Workshop on Transport in Fusion Plasmas* Aspenäs, Göteborg, Sweden

[15] Christiansen J P, Cordey J G and Taroni A 1994 *Nucl. Fusion* **34** 375

[16] Goldston R J, McCune D C, Towner H H, Davis S L, Hawryluk R J and Schmidt G L 1981 *Journal of Comput. Phys* **43**

[17] Nordman H and Weiland J 1993 Invited paper at the U.S.-Japan Workshop on Ion-Temperature-Gradient-Driven Turbulent Transport, Austin Texas

[18] Romanelli F and Zonca F 1993 20th EPS Conf. Controlled Fusion and Plasma Physics, Part IV, 1387

[19] Hinton F L and Hazeltine R D 1976 *Review of Modern Physics* **48** 239

[20] Cenacchi G and Taroni A 1988 *JET-IR(88)03*

[21] D'haeseleer W D, Hitchon W N G, Callen J D and Shohet J L 1991 *Flux Co-ordinates and Magnetic Field Structure* (Springer-Verlag)

[22] Blum J and Le Foll J 1984 *J. Comput. Phys* Rep 1, 465

[23] Springmann E *Flush Users Guide JET-TN*

[24] Lapidus L and Pinder G F 1982 *Numerical Solution of Partial Differential Equations in Science and Engineering* (John Wiley and Sons)

TABLE I	I_p	B_T	$n_e(0)\times10^{19}$	$T_e(0)$	$T_i(0)$	P_{ICRH}	P_{NBI}
	(MA)	(T)	(m^{-3})	(keV)	(keV)	(MW)	(MW)
#17749							
43.9<t<45.9	3.0	3.1	4.9-6.6	4.6-11.8	4.4-9.6	0-12.5	4-5.2
#19691							
52.9<t<55.4	3.0	3.0	4.2-6.5	4.6-6.4	4.6-8.8		10.6-17.8
#19739							
49.2<t<51.0	3.0	3.0	4.4-5.0	8.2-9.2	4.8-6.8	7.6-8.9	2.6
#20981							
48.3<t<51.9	4.0-4.3	3.0	0.9-6.0	3.0-9.0	1.0-22.0		1.0-18.0
#25432							
51.0<t<52.9	3.2	2.9	2.1-5.4	4.0-10.0	6.0-18.0		10-15.6
#26095							
51.0<t<51.7	3.2	2.9	3-3.5	4.0-5.8	3.0-7.8		6.3-7.2
#26705							
45.0<t<45.4	3.1	2.7	10.5	4.5-5.3	4.6-5.8		11.5

Table 1. Main characteristics of the discharges used in the interpretative comparison. The steady-state events were selected within the time interval which is given below each pulse number. The given quantities represent min. and max. values during this interval.

TABLE II	I_p (MA)	B_T (T)	$n_e(0)\times10^{19}$ (m^{-3})	$T_e(0)$ (keV)	$T_i(0)$ (keV)	P_{ICRH} (MW)	P_{NBI} (MW)
#15596							
44.0<t<46.5	3.0	2.9	5.3-7.9	1.2-3.2	1.1-3.0	7.0-7.9	
#19691							
53.0<t<56.0	3.0	3.0	4.2-6.5	4.6-6.4	4.6-8.8		10.6-17.8
#19739							
48.5<t<51.5	3.0	3.0	4.4-5.0	8.2-9.2	4.8-6.8	7.6-8.9	2.6
#27578							
44.2<t<46.4	3.3	2.9	6.0-8.0	4.5-6.3	4.6-5.9	10.2-10.6	
#27654							
47.0<t<50.0	4.0	3.4	4.7-6.3	3.2-7.8	3.4-5.4	0.4-10.2	

Table 2. Main characteristics of the discharges used in the predictive comparison. The simulations were performed using the time interval given below each pulse number. The given quantities represent min. and max. values during this interval.

TABLE III

shot no. time	f_B	$\sigma T_i / T_i$	$\sigma T_e / T_e$	σ_n / n
#15596 44<t<46.5s	1.0 0.75 0.50	0.04 0.06 0.12	0.05 0.08 0.14	0.10 0.10 0.10
#19691 53<t<56s	1.0 0.75 0.50	0.09 0.07 0.06	0.10 0.07 0.05	0.17 0.17 0.15
#19739 48.5<t<51.5s	1.0 0.75 0.50	0.07 0.08 0.11	0.11 0.08 0.06	0.07 0.07 0.07
#27578 44.2<t<46.4s	1.0 0.75 0.50	0.14 0.09 0.05	0.05 0.07 0.10	0.12 0.12 0.12
#27654 47<t<50s	1.0 0.75 0.50	0.08 0.08 0.10	0.06 0.05 0.08	0.08 0.07 0.07

Table 3. Time averaged values of the quality measure $\sigma_{Ti} / T_i, \sigma_{Te} / T_e$ and σ_n / n as defined in equation (46).

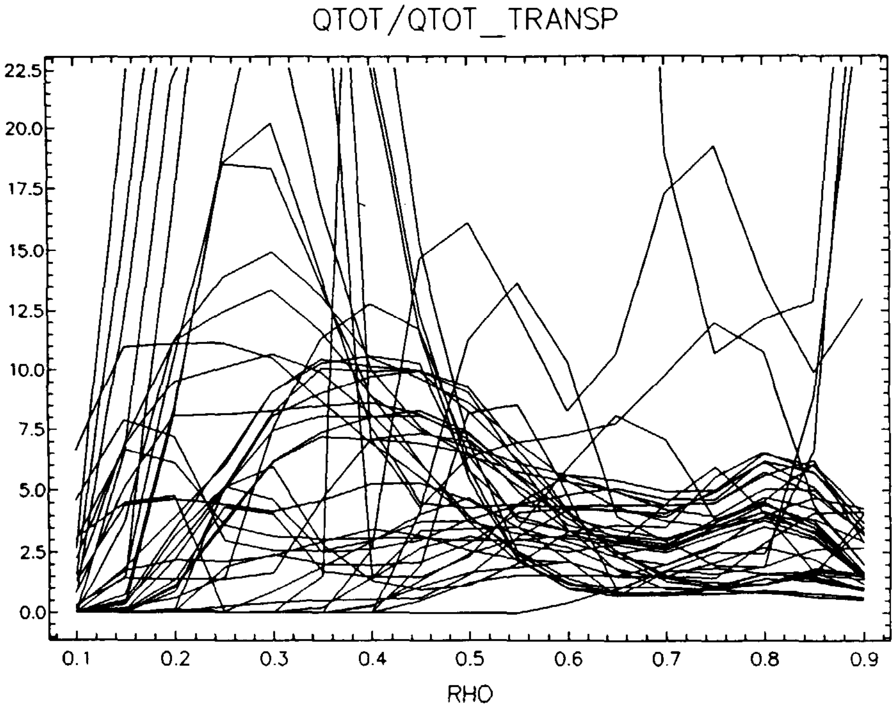

Fig. 1. Ratio of theoretical and experimental total heat fluxes versus the magnetic flux surface coordinate.

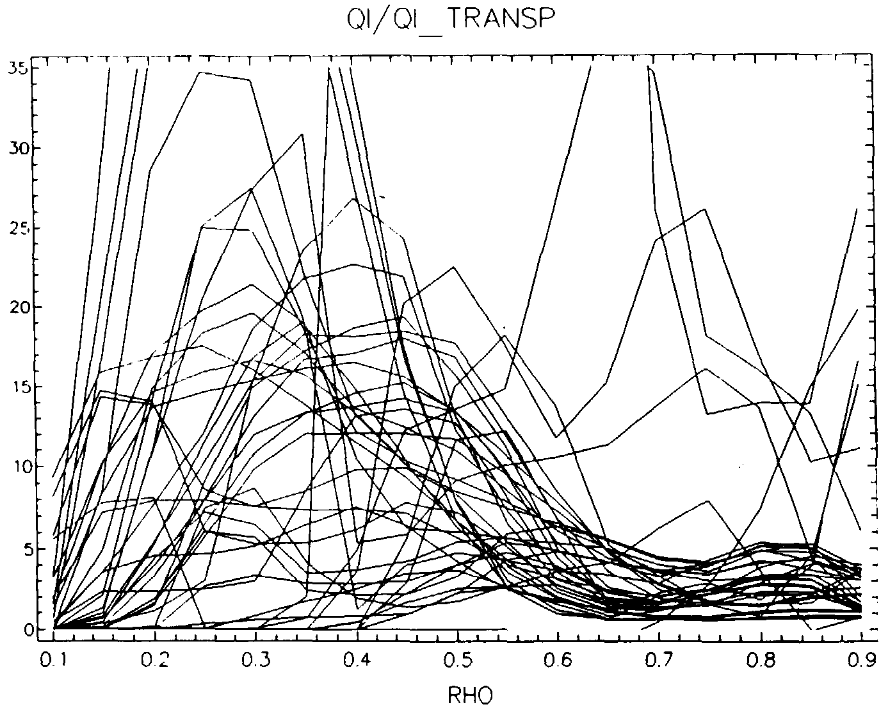

Fig. 2. Ratio of theoretical and experimental ion heat fluxes versus the magnetic flux surface coordinate.

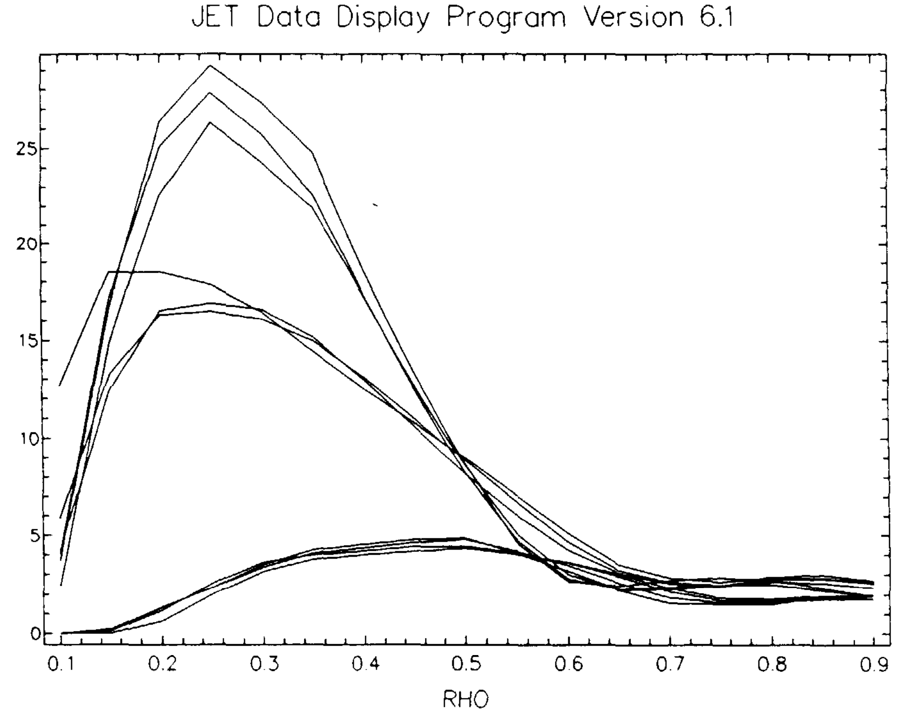

Fig. 3. Ion thermal diffusivity (see (9), the 3/2 was however not included) versus the magnetic flux surface coordinate, for a number of steady-state events in discharge #17749.

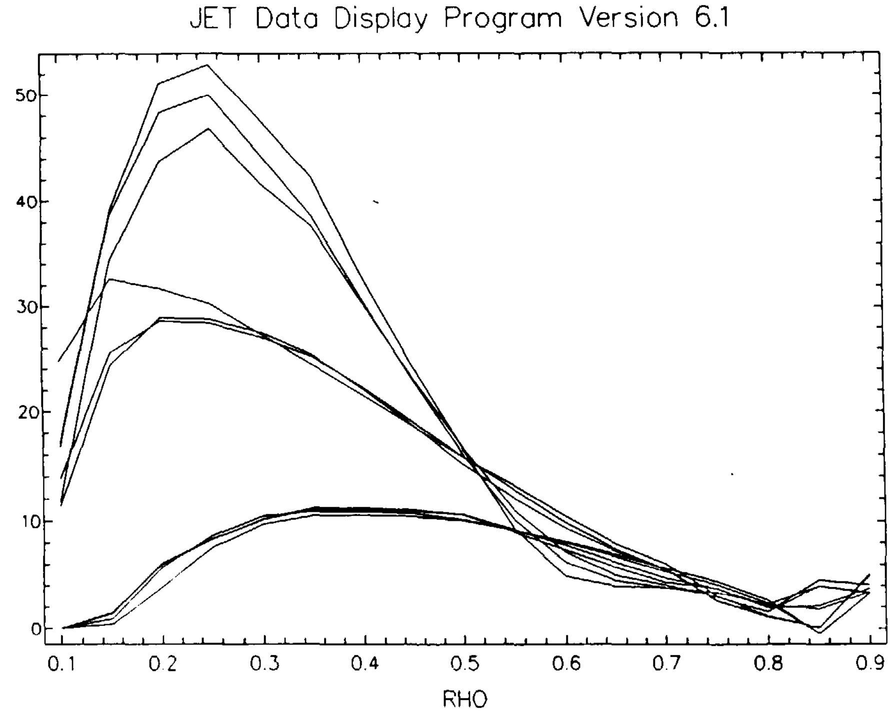

Fig. 4. $(\gamma^3 / k_x^2) / ((\omega_r - \omega_{Di})^2 + \gamma^2)$ versus the magnetic flux surface coordinate, for a number of steady-state events in discharge #17749. The growth rate for the mode in the ion drift direction was used.

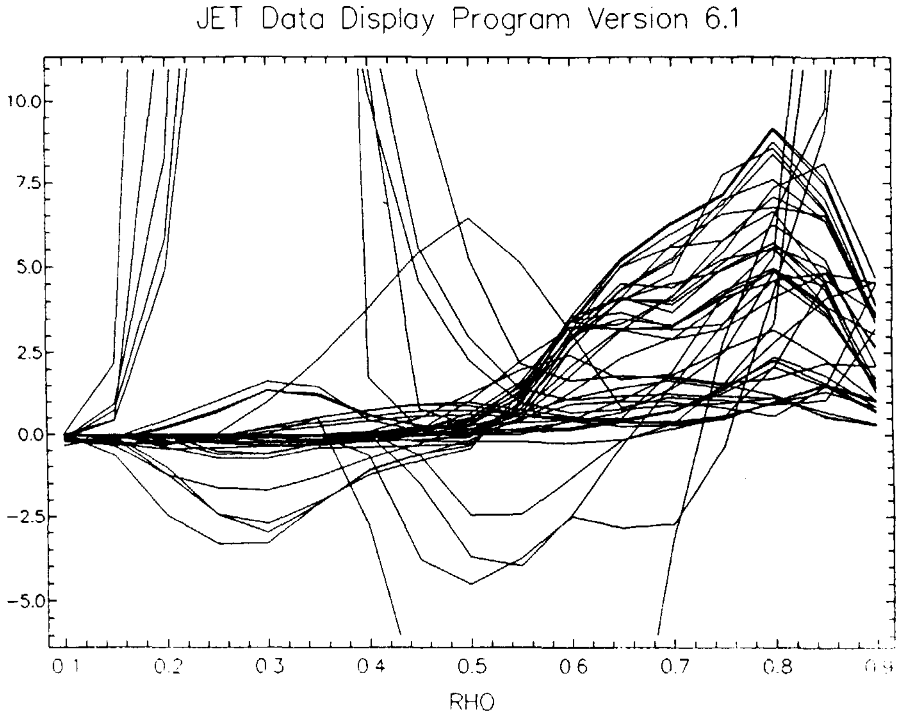

Fig. 5. Ratio of theoretical and experimental electron heat fluxes versus the magnetic flux surface coordinate.

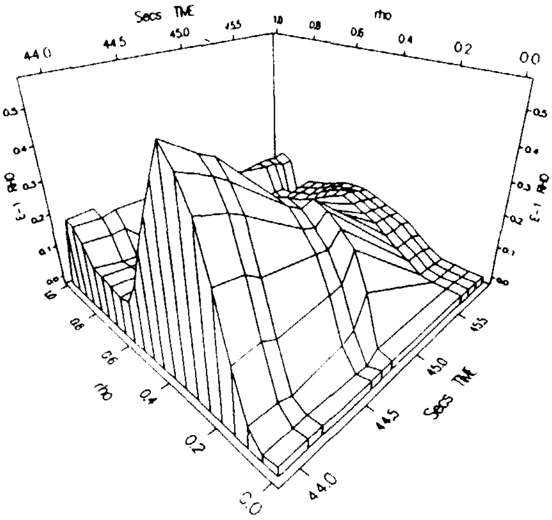

Fig. 6. A saturation level estimate of $|\delta T_i / T_i|$ versus the magnetic flux surface coordinate. The growth rate for the mode in the ion drift direction was used in the estimate.

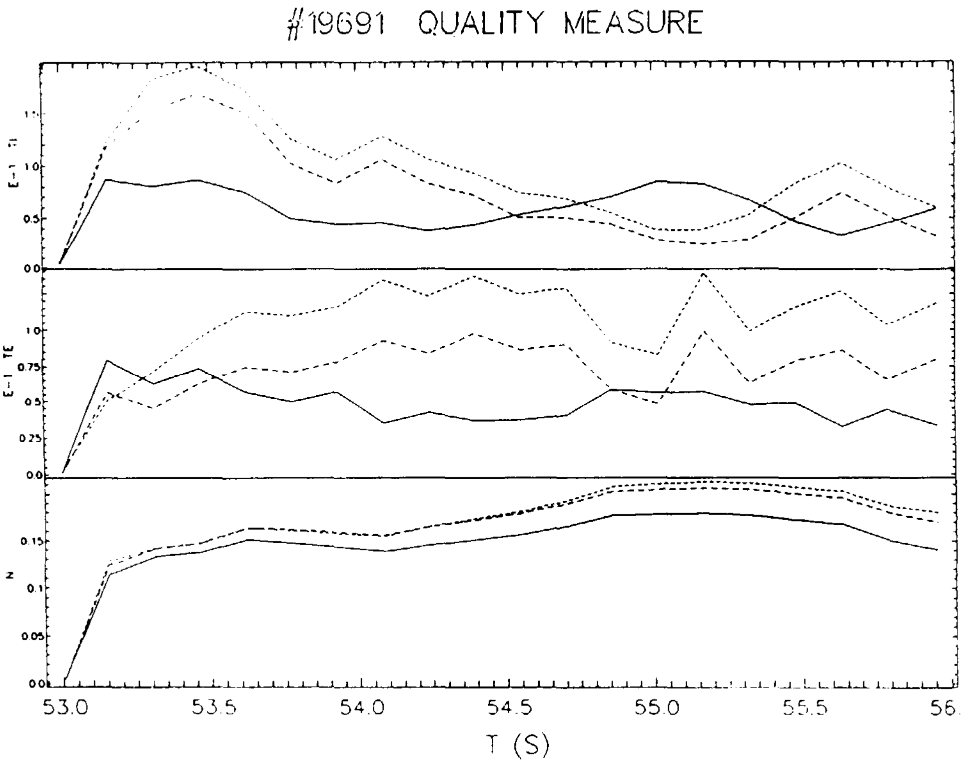

Fig. 7. Time evolution of the quality measures σ_{T_i}/T_i (top), σ_{T_e}/T_e (middle) and σ_n/n (bottom) for shot #19691 with different f_b values.

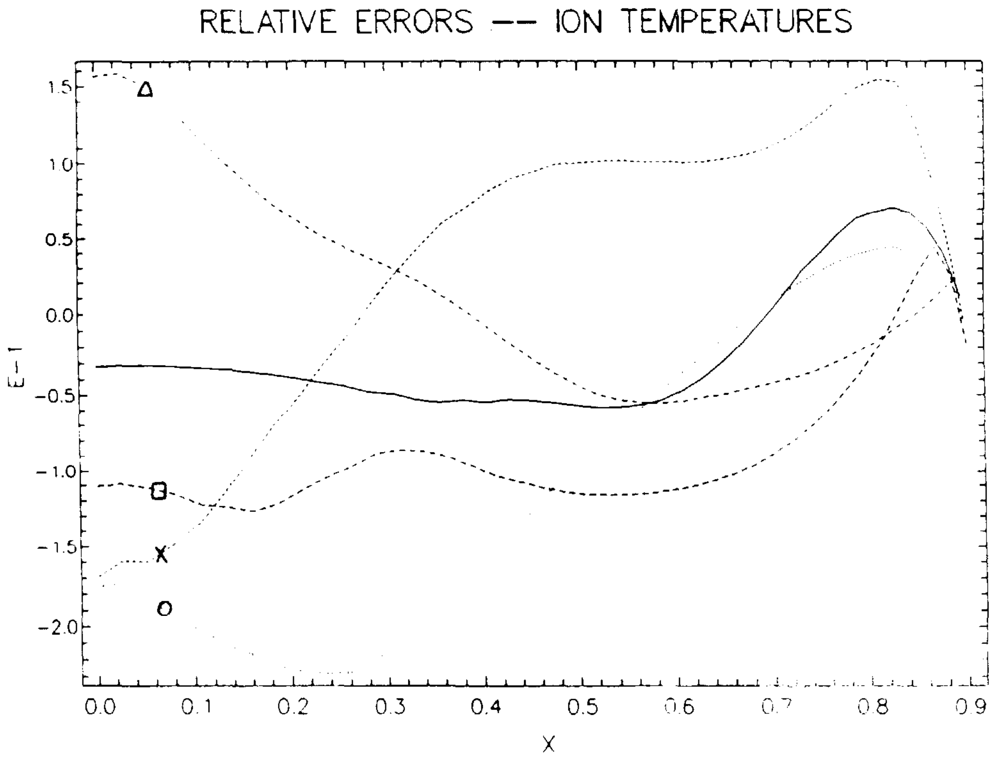

Fig. 8. Relative errors in the ion temperature profile as a function of the normalised minor radius for shots #15596 (—) at t=46.5s, #19691 (□) at t=55.8s, #19739 (×) at t=51.1s, #27578 (O) at t=46.0s and #27654 (Δ) at t=49.5s. The profiles were obtained with a flux surface average factor f_B = 1.0.

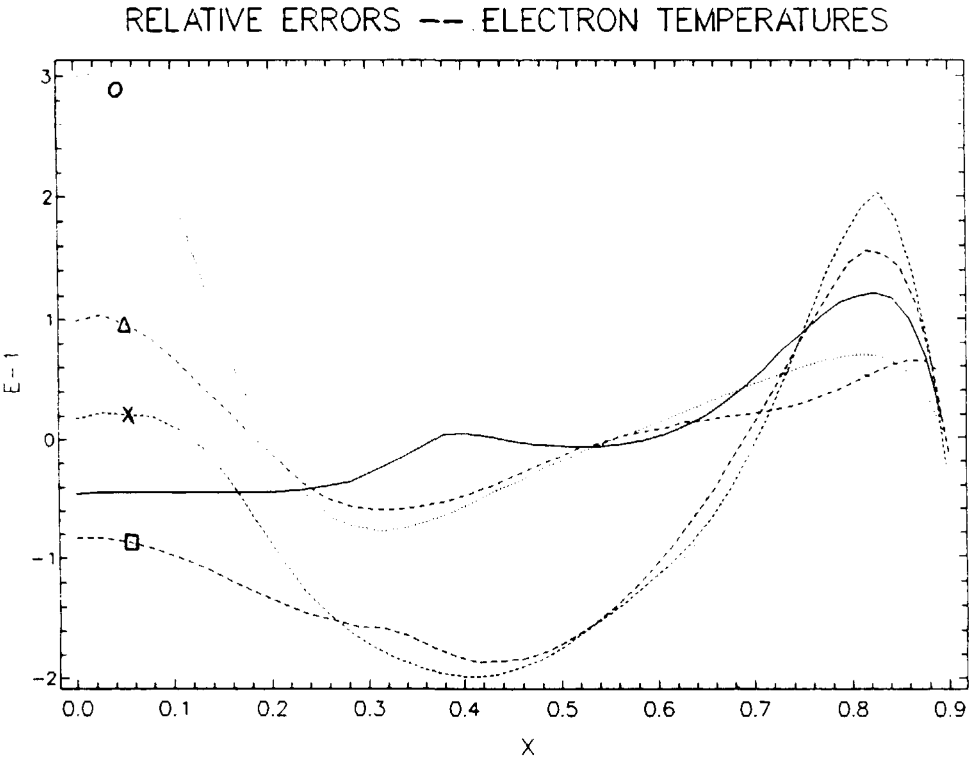

Fig. 9. Relative errors in the electron temperature profile as a function of the normalised minor radius for shots #15596 (––) at t=46.5s, #19691 (□) at t=55.8s, #19739 (×) at t=51.1s, #27578 (O) at t=46.0s and #27654 (Δ) at t=49.5s. The profiles were obtained with a flux surface average factor f_B = 1.0.

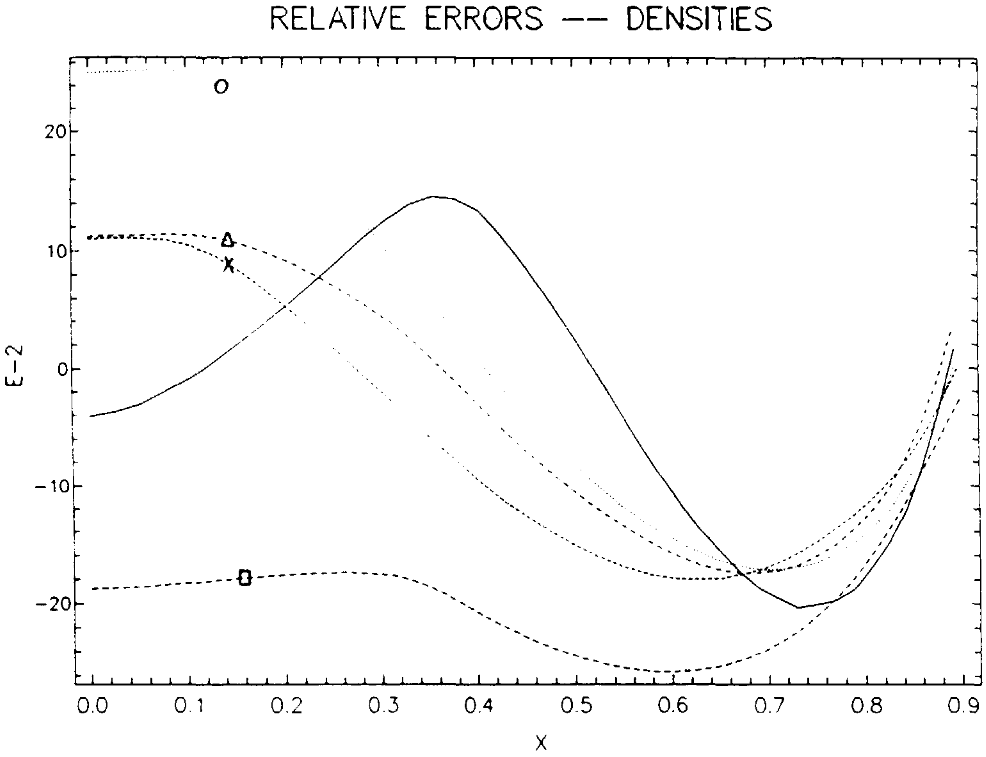

Fig. 10. Relative errors in the density profile as a function of the normalised minor radius for shots #15596 (—) at t=46.5s, #19691 (□) at t=55.8s, #19739 (×) at t=51.1s, #27578 (O) at t=46.0s and #27654 (Δ) at t=49.5s. The profiles were obtained with a flux surface average factor f_B = 1.0.

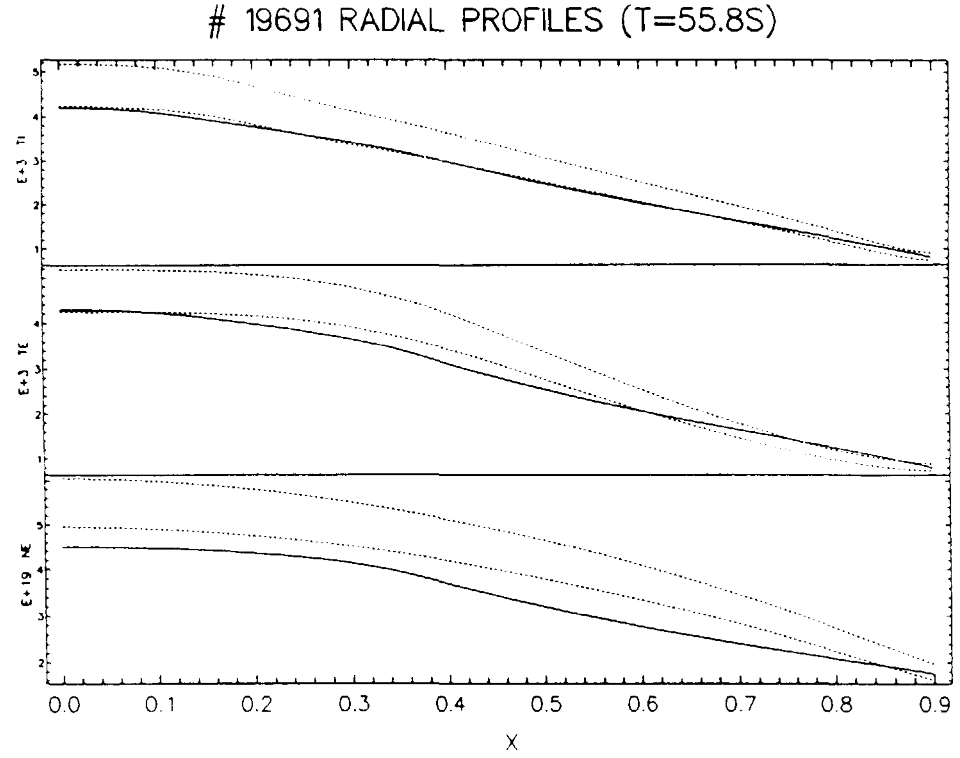

Fig. 11. Ion temperature (top), electron temperature (middle) and density (bottom) profiles shown together with upper and lower 10% error estimates of the profiles as obtained from TRANSP, for shot #19691. The experimental time = 55.8s which corresponds to 2.8s in the simulation. The profiles were obtained with a flux surface averaging factor f_B = 1.0.

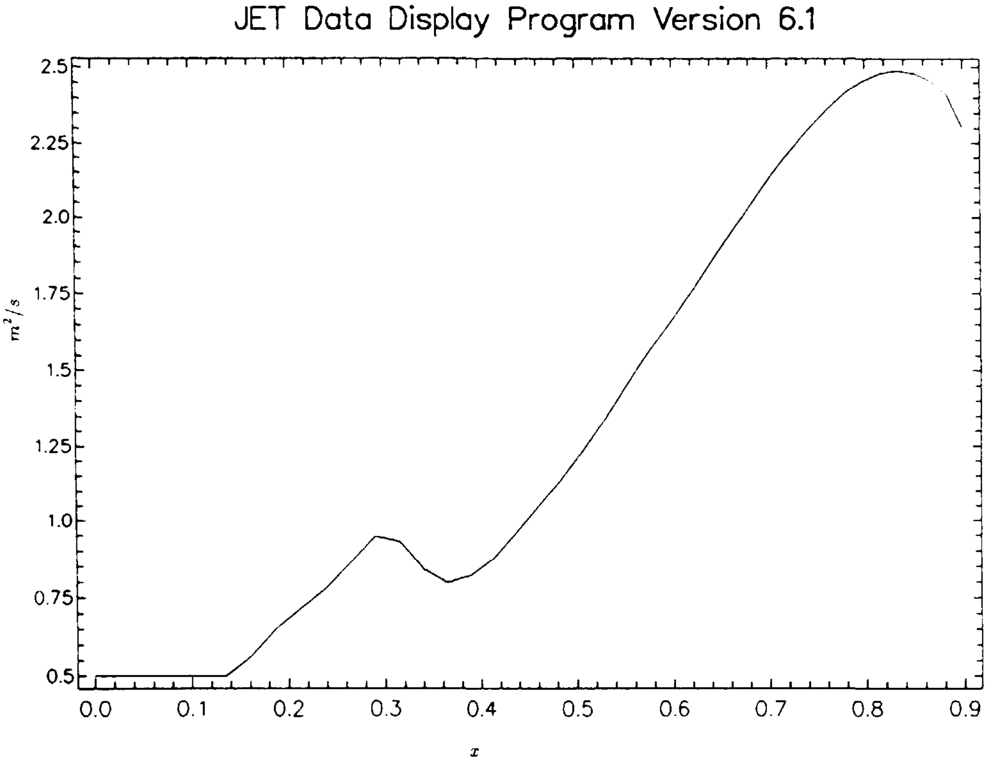

Fig. 12. The effective ion thermal diffusivity as a function of normalised minor radius for shot #19691 at t=55.8s.